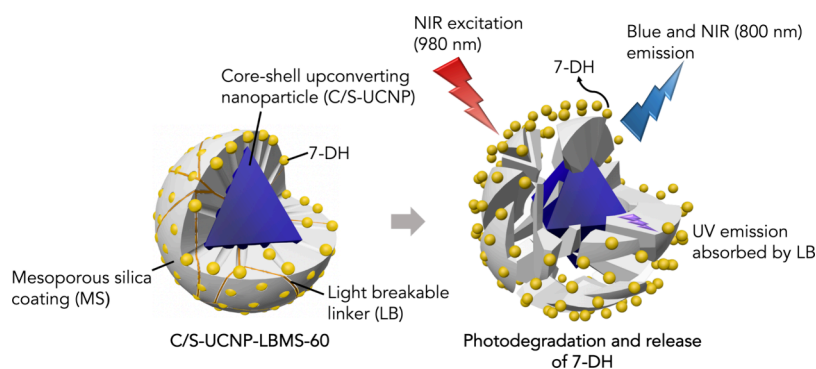# Upconverting Nanoparticles Coated with Light-Breakable Mesoporous Silica for NIR-Triggered Release of Hydrophobic Molecules

Vivienne Tam, Pierre Picchetti, Yiwei Liu, Artiom Skripka, Marco Carofiglio, Giulia Tamboia, Arianna Bresci, Francesco Manetti, Giulio Cerullo, Dario Polli, Luisa De Cola, Fiorenzo Vetrone, and Marta Cerruti*

ABSTRACT: Upconverting nanoparticles (UCNPs) doped with Yb^{3+} and Tm^{3+} are near-infrared (NIR) to ultraviolet (UV) transducers that can be used for NIR-controlled drug delivery. However, due to the low quantum yield of upconversion, high laser powers and long irradiation times are required to trigger this drug release. In this work, we report the one-step synthesis of a nanocomposite consisting of a $LiYbF_4:Tm^{3+}@LiYF_4$ UCNP coated with mesoporous UV-breakable organosilica shells of various thicknesses. We demonstrate that a thin shell accelerates the breakage of the shell at $1\ W/cm^2$ NIR light exposure, a laser power up to 9 times lower than that of conventional systems. When the mesopores are loaded with hydrophobic vitamin D_3 precursor 7-dehydrocholesterol (7-DH), shell breakage results in subsequent cargo release. Its minimal toxicity in HeLa cells and successful internalization into the cell cytoplasm demonstrate its biocompatibility and potential application in biological systems. The tunability of this system due to its simple, one-step synthesis process and its ability to operate at low laser powers opens up avenues in UCNP-powered NIR-triggered drug delivery toward a more scalable, flexible, and ultimately translational option.

KEYWORDS: upconversion, light-controlled, drug delivery, translational, mesoporous silica

INTRODUCTION

Light can be used to trigger drug delivery non-invasively with high spatiotemporal resolution.[1] However, while ultraviolet (UV) light provides sufficient energy for the cleavage of the linker to occur, large doses of UV light are carcinogenic.[2] Also, UV has a limited tissue penetration depth[3] (~61 μm) caused by tissue scattering and tissue absorption,[4] preventing UV light from reaching organs below the skin.[5] Near-infrared (NIR) radiation, on the contrary, is noncarcinogenic and provides sufficient tissue penetration (~3.2 cm).[6] However, low-energy NIR radiation is insufficient to trigger the breakage of photolabile bonds.

Lanthanide-doped upconverting nanoparticles (UCNPs) have the potential to solve this central challenge. They have been developed as NIR to UV transducers, as they convert noncarcinogenic NIR irradiation into high-energy photons in

the UV−visible (UV−vis) region via a photon upconversion process.[7,8] When combined with a photolabile drug carrier, they produce a system in which drugs can be released on demand using NIR irradiation.

The low quantum yield of upconversion (<1%)[9] limits the clinical translation of UCNP-powered drug delivery, because high laser powers and long irradiation times[9−12] are often necessary to generate sufficient upconverted UV radiation to

break UV-breakable bonds, and this may overheat tissues exposed to the lasers. The main strategies employed so far to solve this problem include passivating the core surface with an inert shell to increase the quantum yield[13,14] and individually coating the UCNPs with the photolabile drug carrier to allow more efficient energy transfer from the UCNP to the photolabile bonds.[15−18] These drug carriers are either mesoporous silica (MS) or polymer coatings.

UCNP-MS systems have several advantages. MS is a well-studied, robust drug carrier that can be synthesized in a simple, one-step procedure.[19−21] It has a high loading capacity for small molecules,[22] a surface that can be easily functionalized,[9] and silica-based degradation products that are biocompatible.[23] However, the UCNP-MS systems currently developed for the delivery of small molecules operate at parameters that are far from optimal. For example, photoisomerizable compounds such as azobenzene, which undergo a physical change under light exposure, have been incorporated into the mesopores.[24] In these systems, high laser powers ($\sim$9 W/cm^2) and long irradiation times (18 h for 80% release)[5] are required to generate sufficient energy to mechanically propel the stirrers. Alternatively, photodegradable molecules such as nitrobenzyl groups have been added as pore gatekeepers that are broken up with the upconverted UV light.[25,26] Once the gatekeeper is removed, however, drug release is driven by uncontrolled passive diffusion, which causes long lag times between irradiation and drug release (20 h for 75% release).[25] Gatekeeper ruthenium complexes are an exciting development in the field that allow for uncapping of the pores at a lower NIR power density (0.7 W/cm^2);[27] however, the NIR stimulus still controls only the start of the release (i.e., the removal of the gatekeeper molecule), while the rest of the release is driven by passive diffusion.

Unlike the UCNP-MS systems described above that remain intact during drug release, UCNPs with a surface-coated polymer are designed with UV-breakable bonds within the polymer itself, causing its structural breakdown and subsequent drug release.[16,28] For example, Jalani et al. demonstrated that via integration of a UV-labile cross-linker within a hydrogel coating around the UCNPs it was possible to release $\sim$92% of the bovine serum albumin loaded within the hydrogel after irradiation for 12 min[28] at 1.8 W/cm^2. There were two drawbacks of this system, however. First, it could entrap only large, hydrophilic macromolecules as small molecules would escape the polymer hydrogels[29] and hydrophobic molecules would not be loadable within the hydrogel; this is a serious disadvantage, because hydrophobic drugs account for >40% of marketed drugs and $\sim$60% of therapeutic compounds at the research and development stage.[30] Second, it required five individual synthesis steps to functionalize the UCNP surface with the photoresponsive hydrogel. This complex synthesis procedure limits its scalability and reproducibility for further translation.

To overcome these challenges, in this work we encapsulate individual UCNPs with a thin, UV-breakable MS shell to harness both advantages of MS as a scalable, simple to fabricate, and highly tunable drug carrier for small molecules and a breakable individual coating as in Jalani's system.

We coated LiYbF$_4$:Tm^{3+}/LiYF$_4$ core/shell UCNPs (C/S-UCNPs) with a light-breakable (LB) MS shell containing UV-responsive nitrobenzyl moieties in a simple one-step procedure following that was recently reported for the synthesis of UV-breakable MS NPs.[31] We show that the UCNP core efficiently converts NIR light to the UV light required to break the nitrobenzyl chains in the MS shell and that this in turn causes the release of a small hydrophobic molecule, vitamin D$_3$ precursor 7-dehydrocholesterol (7-DH), entrapped in the MS pores. When the UCNPs are coated with a thin (10 nm) LBMS shell, irradiation with a laser power of 1 W/cm^2 for 2 h is sufficient to release 44% of the 7-DH entrapped in the pores.

These results show the effectiveness of thin individual UV-breakable UCNP-MS coatings in decreasing the laser power required for NIR-triggered drug release, expand the versatility of UCNP-based drug delivery systems to include hydrophobic drugs, and increase the scalability and reproducibility by minimizing the number of synthesis steps. These are all crucial steps toward the clinical translation for UCNPs.

MATERIALS AND METHODS

Materials. Y$_2$O$_3$ (REacton, 99.999%), Yb$_2$O$_3$ (REacton, 99.998%), Tm$_2$O$_3$ (REacton, 99.999%), trifluoroacetic acid (99%), 1-octadecene (ODE, 90%), and oleic acid (OA, 90%) were purchased from Alfa Aesar. Lithium trifluoroacetate (LiCO$_2$CF$_3$, 98%), oleylamine (OM, 70%), cetyltrimethylammonium bromide (CTAB, ≥99%), tetraethyl orthosilicate (TEOS, >99%), ethanol (EtOH), chloroform (CLF, >99%), sodium hydroxide (NaOH, >98%), hydrochloric acid (HCl, 37%), acetone (>99.5%), hexane (>95%), sodium hydride (NaH, 90%), 5-hydroxy-2-nitrobenzyl alcohol, 97%), *N,N*-dimethylformamide (DMF, anhydrous, 99.8%), triethoxysilane (95%), platinum(0)-1,3-divinyl-1,1,3,3-tetramethyldisiloxane complex solution (Karstedt's catalyst; $\sim$2 wt % Pt in xylene), allyl bromide (97%), sodium sulfate (anhydrous, Na$_2$SO$_4$, >99%), (3-aminopropyl)triethoxysilane (APTES, 99%), and sodium hydrogen carbonate (Na$_2$CO$_3$, >99.7%) were obtained from Sigma-Aldrich. Sulfo-Cyanine5 NHS ester (Cy5) was obtained from Lumiprobe. 3-(4,5-Dimethyl-2-thiazolyl)-2,5-diphenyl-2*H*-tetrazolium bromide (MTT), fetal bovine serum (FBS), and Dulbeccco's modified Eagle's medium (DMEM) were obtained from Gibco. L-Glutamine and 1% penicillin/streptomycin were obtained from Euroclone. Alexa Fluor 568 Phalloidin, Triton X-100, 4′,6-diamidino-2-phenylindole (DAPI), formalin (10%), and bovine serum albumin (BSA) were obtained from ThermoFisher. Compressed argon gas was obtained from Linde Gas at >99.9% purity.

Synthesis of Core/Shell LiYbF$_4$:Tm^{3+}/LiYF$_4$ (C/S-UCNP). UCNP synthesis was performed using a protocol previously developed by Cheng et al.[7] The following steps are described in more detail below: (a) preparation of rare earth (RE) trifluoroacetate precursors, (b) synthesis of LiYbF$_4$:Tm^{3+} first nuclei (FN), (c) stabilization of FN to form core UCNP (C-UCNP), and finally (d) shelling of FN with a passive LiYF$_4$ shell to form the core/shell UCNP (C/S-UCNP).

Precursor Preparation. RE trifluoroacetate precursors were prepared by mixing RE$_2$O$_3$ (RE = Yb, Y, or Tm) with 10 mL of a trifluoroacetic acid/distilled water mixture [1/1 (v/v)] in a 50 mL three-neck round-bottom flask. To synthesize the precursors for 2.5 mmol of LiYbF$_4$:Tm^{3+} (0.5%) first nuclei (FN), 1.1875 mmol (467.97 mg) of Yb$_2$O$_3$ and 0.00625 mmol (2.4 mg) of Tm$_2$O$_3$ were used. In a separate three-neck flask, 2.5 mmol (564.5 mg) of Y$_2$O$_3$ was used to synthesize the precursors for 2.5 mmol of the LiYF$_4$ passive shell. For each flask, the slurry was refluxed under vigorous stirring at 80 °C until a clear solution formed. The temperature was then decreased to 60 °C to evaporate the solvent until the solution was dry. The obtained dried solids in the flask with Yb and Tm were used as precursors for the synthesis of FN, while the Y shelling precursors were stored until the shelling of the stabilized FN.

Synthesis of LiYbF$_4$:Tm^{3+} First Nuclei (FN). Two solutions were prepared for the synthesis of FN. Solution A, a mixture of 7 mL of OA, 7 mL of OM, and 14 mL of ODE, was prepared in a 100 mL three-neck round-bottom flask. Solution A was stirred and degassed under a vacuum at 110 °C for 30 min first. Then, its temperature was increased to 330 °C under an Ar atmosphere. Meanwhile, solution B

was prepared. Solution B was a mixture of 2.5 mmol of LiCO$_2$CF$_3$, dried Yb and Tm precursors synthesized above, 3 mL of OA, and 6 mL of ODE prepared in a 50 mL three-neck round-bottom flask. Solution B was then degassed under vacuum at 110 °C for 30 min. After the dried precursors were dissolved under vacuum in an OA/ODE mixture, 3 mL of OM was added to solution B. Once solution A had reached the stable desired temperature of 330 °C, solution B was injected into solution A using a pump-syringe system (Harvard Apparatus, Pump 11 series) with an injection rate of 1.5 mL/min. After being stirred for 1 h at 330 °C, the reaction mixture was cooled to room temperature under an Ar atmosphere. The majority of the synthesized product was stored in a Falcon centrifuge tube (50 mL) under Ar, while a small portion (0.1 mL) of the product was washed for structural characterization by first precipitation with acetone, centrifugation at 8000 rcf for 15 min (OHAUS FC5718 Frontier 5000 Series), then washing with a hexane/acetone mixture [1/4 (v/v)] twice, and finally redispersion in hexane for TEM preparation.

Stabilization of LiYbF$_4$:Tm^{3+} FN (C-UCNP). To stabilize the sub-10 nm FN cores that were synthesized in the presence of a high concentration of OM, it was necessary to add a stronger coordinating ligand, such as OA, for slightly larger but thermodynamically stable UCNPs, which we call C-UCNP. As the FN solidified after storage at room temperature, the Falcon tube was placed in a 40 °C water bath to return it to its liquified form. Then, 1.1 mmol of FN obtained in the step described above was mixed with OA and ODE [1/1 (v/v)] for a total final volume of 40 mL. The solution was stirred and degassed under vacuum at 110 °C for 30 min. Then the temperature of the solution was increased and maintained at 315 °C for 1 h under an Ar atmosphere. After cooling to room temperature, C-UCNP was stored in a Falcon centrifuge tube (50 mL) under Ar for further shelling. A small portion (0.1 mL) of C-UCNP was washed as described above for TEM preparation.

LiYF$_4$ Shelling for Core/Shell LiYbF$_4$:Tm^{3+}/LiYF$_4$ (C/S-UCNP). To maximize the upconversion emission and reduce the energy loss to the surrounding ligands, the stabilized cores were shelled with a LiYF$_4$ passive shell. Again, two solutions were prepared. Solution A was prepared in a 100 mL three-neck round-bottom flask. C-UCNP was heated in a 40 °C water bath until it was liquefied, and 0.18 mmol of C-UCNP was added to solution A with equal volumes of OA and ODE to reach a final volume of 20 mL. Solution B consisted of 2.5 mmol of the shelling precursors (Y$_2$O$_3$) as already prepared in the Precursor Preparation section, 309 mg of LiCO$_2$CF$_3$, and 10 mL each of OA and ODE for a final volume of 20 mL. Both solutions were stirred and degassed under vacuum at 110 °C for 30 min. After the degassing procedure, solution A was placed under an Ar atmosphere and the temperature increased to 315 °C. Solution B was injected into solution A at an injection rate of 1 mL/min under vigorous magnetic stirring. After injection, the mixture was kept at 315 °C and allowed to react for 1 h with continuous vigorous stirring. Subsequent steps included cooling to room temperature and washing as described for FN synthesis. Shelled LiYbF$_4$:Tm^{3+}/LiYF$_4$ C/S-UCNP was stored in 20 mL of hexane in a glass vial (60−65 mg/mL).

Synthesis of Mesoporous Silica-Coated Upconverting Nanoparticles (C/S-UCNP-MS). C/S-UCNP-MS were synthesized using a protocol adapted from ref 32. Seven milligrams of C/S-UCNP in hexane as described above was first precipitated with EtOH and redispersed in 167 μL of chloroform. In a separate 20 mL glass vial, 16.7 mg of CTAB was dissolved in 3.33 mL of deionized water and heated at 70 °C in a preheated oil bath until clear. Then, the dispersed C/S-UCNP in chloroform was added to the CTAB solution at room temperature, vortexed until it was milky in appearance, sonicated for 10 min, and stirred at 400 rpm for 20 min. The mixture was then transferred to the oil bath at 70 °C under magnetic stirring at 400 rpm for 15−20 min until the mixture formed a transparent suspension.

Next, 6.67 mL of water, 1 mL of EtOH, 50 μL of 2 M NaOH, and the transparent C/S-UCNP suspension (3.5 mL) from above were added to a three-neck 100 mL round-bottom flask. The three-neck flask was then heated under reflux at 70 °C, with stirring at 1000 rpm for 5 min. Then, 66.7 μL of TEOS was pipetted into the suspension in fractionated drops, with each drop to be at ∼10 μL, spaced 10 s apart.

The suspension was left to stir under reflux for 10 min before being transferred into an ice bath to stop silica network formation. The amount of TEOS added was adjusted to vary the silica shell thickness, ranging from 60 to 100 volume %, with 100% representing the original volume used (66.7 μL). For example, C/S-UCNP-MS-60 was used to denote the particles synthesized with 40 μL of TEOS; 100% TEOS volume corresponded to a UCNP/TEOS mass ratio of 1/9.

The C/S-UCNP-MS suspension was precipitated with EtOH, centrifuged at 4500 rpm for 20 min, then washed once with an EtOH/acetone mixture [1/1 (v/v)], and redispersed in 10 mL of EtOH. To remove the CTAB from the mesopores, 10 μL of HCl was added to the C/S-UCNP-MS suspension and left to reflux overnight under magnetic stirring (400 rpm) at 90 °C. After reflux, the suspension was centrifuged to remove the extracted CTAB and redispersed in 10 mL of EtOH. To measure the concentration, an empty Eppendorf tube was weighed, and 1 mL of the C/S-UCNP-MS suspension was dried under vacuum overnight at room temperature. After the suspension was dried, the Eppendorf tube with dried C/S-UCNP-MS was weighed again, and the difference in mass was then divided by the initial volume (i.e., 1 mL) to obtain the final concentration.

Synthesis of the Light-Breakable Linker (LB). The synthesis of the light-breakable linker (LB) was adapted from a previously established synthesis by Picchetti et al.[6] In the first step, the diallyl derivative of 5-hydroxy-2-nitrobenzyl alcohol (Compound 1) was prepared by the addition of NaH (311 mg, 12.98 mmol) to a stirring solution of 5-hydroxy-2-nitrobenzyl alcohol (1.00 g, 5.91 mmol) in dry DMF (10 mL) at 0 °C. After complete NaH addition, the reaction mixture was allowed to stir for a further 10 min at 0 °C. Subsequently, allyl bromide (1.17 mL, 13.52 mmol) was added dropwise to the stirring reaction mixture at 0 °C. The reaction mixture was stirred for 1 h at 0 °C and for a further 1 h at room temperature before the reaction was quenched with 5 mL of water. The aqueous layer was extracted with ethyl acetate (3×, 20 mL), and the organic layers were washed with a saturated Na$_2$CO$_3$ solution before being dried over anhydrous Na$_2$SO$_4$. The solvent was then evaporated under reduced pressure, and the crude oil purified by column chromatography (silica gel, 1/2 EtOAc/cyclohexane), yielding Compound 1 as a yellowish oil (yield of 68%): ^{1}H NMR (CDCl$_3$, 400 MHz) δ 8.16 (d, 1H, J = 9.1 Hz), 7.37 (m, 1H), 6.87 (m, 1H), 6.08−5.95 (m, 2H), 5.46−5.25 (m, 4H), 4.94 (s, 2H), 4.66−4.64 (m, 2H), 4.17−4.15 (m, 2H); ^{13}C{^{1}H} NMR (CDCl$_3$, 100 MHz) δ 163.0, 139.9, 139.0, 134.2, 132.0, 127.6, 118.6, 117.3, 113.5, 113.3, 71.9, 69.3, 69.0.

A light-breakable bis-alkoxysilane, triethoxy[3-(4-nitro-3-{[3-(triethoxysilyl)propoxy]methyl}phenoxy)propyl]silane (LB), was obtained via dihydrosilylation of Compound 1 using triethoxysilane and the hydrosilylation catalyst. Briefly, to the product obtained above (1.00 g, 4.01 mmol) in dry toluene (9 mL), triethoxysilane (2.02 mL, 10.95 mmol), and platinum(0)-1,3-divinyl-1,1,3,3,-tetramethyldisiloxane complex solution (Karstedt's catalyst, ∼2 wt % Pt in xylene, 125 μL) were added dropwise. The reaction mixture was stirred at 50 °C for 12 h. Additional Karstedt's catalyst solution (100 μL) was added, and the mixture was stirred for a further 12 h at 50 °C. The organic solvent was evaporated under reduced pressure, and the crude oil was purified with column chromatography (silica gel, 1/7). EtOAc/cyclohexane), yielding LB as a yellowish oil (yield of 60%): ^{1}H NMR (400 MHz, CDCl$_3$) δ 8.14 (d, 1H, J = 9.1 Hz), 7.31 (m, 1H), 6.83 (m, 1H), 4.90 (s, 2H), 4.04 (t, 2H, J = 6.7 Hz), 3.86−3.81 (m, 12H), 3.58 (t, 2H, J = 6.8 Hz), 1.97−1.90 (m, 2H), 1.84−1.77 (m, 2H), 1.23 (t, 18H, J = 7.0 Hz), 0.79−0.75 (m, 2H), 0.73−0.69 (m, 2H); ^{13}C{^{1}H} NMR (CDCl$_3$,100 MHz) δ 163.6, 139.6, 139.4, 127.6, 113.3, 112.8, 73.5, 70.5, 69.6, 58.5, 58.4, 23.1, 22.7, 18.3, 6.6, 6.5. NMR spectra are shown in Figures S1 and S2.

Synthesis of Light-Breakable Mesoporous Silica-Coated Upconverting Nanoparticles (C/S-UCNP-LBMS). The synthesis protocol was identical to the protocol for C/S-UCNP-MS described above, with the only change being the addition of the LB linker to the TEOS before its addition to the UCNP suspension. A 80 mol %/20 mol % (i.e., 1.55 μL of TEOS/mg of LB linker) TEOS/LB linker mixture was prepared and pipetted up and down until the sample

became homogeneous. The volumes of these mixtures were adjusted on the basis of the TEOS volume percent used to make shells of various thicknesses. For example, for C/S-UCNP-LBMS-100, 53 μL of TEOS, which corresponds to 80% of 66.7 μL, and 34.5 mg of the LB linker were added. C/S-UCNP-LBMS-60 denotes that 32 μL of TEOS and 20.7 mg of the LB linker were added. After the synthesis, C/S-UCNP-LBMS were refluxed, centrifuged, washed, and redispersed as reported above for the C/S-UCNP-MS.

NIR- and UV-Triggered Degradation of C/S-UCNP-LBMS. To assess the ability of the C/S-UCNP-LBMS to break upon exposure to NIR, C/S-UCNP-LBMS-60 and C/S-UCNP-LBMS-100 were dispersed in a 1/1 (v/v) EtOH/water mixture with a concentration of 0.5 mg/mL and exposed to 980 nm irradiation (1 W/cm^2) while being stirred at 400 rpm. The ethanol/water mixture was used to ensure that the observed degradation was not due to hydrolysis of silica, which can occur in pure water. UV−vis absorption spectra and TEM images were taken at different time points to track degradation of the LB linker and LBMS shells.

This experiment was repeated three times under the same conditions, and the average of the 320 nm peak height and the standard deviation are reported.

UV exposure experiments were performed using a Philips PL-S 9W UV-A lamp that had a broad emission wavelength between 315 and 380 nm. The 1/1 (v/v) EtOH/water suspension of C/S-UCNP-LBMS-60 was placed directly next to the lamp and stirred at 400 rpm.

7-DH Loading and NIR-Triggered Release. To load 7-DH, 5 mg of C/S-UCNP-LBMS was suspended in 200 μL of EtOH with 40 mg of 7-DH and sonicated for 15−30 min before drying under vacuum overnight. Then, they were washed three times with 2 mL of EtOH and dried again overnight.

To study the release, 400 μL of an aqueous dispersion of C/S-UCNP-LBMS at a concentration of 2.5 mg/mL was placed in a 3.5 mL quartz cuvette (10 mm path length) equipped with a small stir bar. A layer of cyclohexane (1 mL) was added on top of the aqueous C/S-UCNP-LBMS dispersion to extract the hydrophobic compound released upon irradiation. This organic layer was sampled during UV−vis measurements.

While being stirred at 100 rpm, the bottom aqueous suspension was irradiated at 980 nm with a power density of 1 W/cm^2, and the change in absorbance at λ = 281 nm in the upper organic phase was monitored over time to track the amount of 7-DH released from the C/S-UCNP-LBMS. Cyclohexane was used for a baseline measurement. Release measurements were repeated with three samples under the same conditions. The mean drug release amount and standard deviation among the trials are reported.

In Vitro Biocompatibility. C/S-UCNP-LBMS-60 were tested in terms of biocompatibility with the HeLa cell line (ATCC, CCL-2), an epithelial-like tumoral cell line that is often exploited for preliminary biocompatibility tests. Cells were cultured with DMEM with 10% (v/v) FBS, 1% L-glutamine, and 1% penicillin/streptomycin (100 μg/mL streptomycin and 100 units/mL penicillin), at 37 °C in a 5% CO$_2$ atmosphere. The viability of the cells following the administration of the NPs was tested through the colorimetric Cell Proliferation Kit I (MTT) metabolic assay (Sigma-Aldrich). Specifically, 4000 cells dispersed in 100 μL of DMEM were seeded in each well of a 96-well plate (treated with TC, Euroclone). After 24 h, the cell culture medium was replaced with NP-containing medium at concentrations of 100, 50, 25, and 12.5 μg/mL. The biocompatibility of C/S-UCNP-LBMS-60 was compared to those of C/S-UCNP-MS-60 and C/S-UCNP-LBMS-60 loaded with 7-DH.

The MTT assay was performed as follows. At the stated incubation time (1, 4, 24, and 48 h after NP administration), the medium in the wells was replaced with 0.5 mg/mL concentrated MTT labeling reagent (according to the producer's specification) dispersed in fresh culture medium. After incubation at 37 °C for 3 h, the medium was withdrawn, leaving on the bottom of the well the nonsoluble formazan crystals resulting from the metabolic activity of cells. The crystals were solubilized with a 0.04 M HCl isopropanol solution, and the absorbance at 565 nm of the liquid inside the wells was measured by an Infinite M200 plate reader (Tecan). The absorbance of each

sample was background subtracted and compared to that of untreated cells (100% cell viability).

Visualization of Cell Internalization via Confocal Microscopy. The internalization of C/S-UCNP-LBMS-60 was analyzed with confocal microscopy by labeling the NPs with Cy5. To do this, 0.5 mg of sulfo-cyanine5 NHS ester (Cy5) was dispersed in 400 μL of anhydrous DMSO under an Ar atmosphere. Then, 4.5 μL of APTES was added to the solution, and the mixture left to stir for 1 h. Eight microliters of the Cy5 solution was added to 1 mL of an aqueous solution of the amine-functionalized C/S-UCNP-LBMS-60 (1 mg/mL) and left to stir overnight for the amine group to react with the NHS ester, forming an amide bond. The NPs were washed three times via centrifugation and redispersion (14000g for 30 min) and finally redispersed at a concentration of 1 mg/mL in distilled water.

To perform confocal microscopy, sterile borosilicate glass slides were placed in the wells of a 24-well plate (tissue culture treated, Euroclone). Subsequently, 3×10^4 HeLa cells dispersed in 500 μL of cell culture medium were placed in each well to allow the cells to grow over the glass. After 24 h, the cell culture medium was replaced with NP-containing medium at concentrations of 100, 50, 25, and 12.5 μg/mL and cultured at 37 °C for 1, 4, 24, and 48 h from the time of NP administration.

After the designated incubation time, the cells were fixed by replacing the cell culture medium with formalin (10%, buffered) for 30 min and washing three times with a phosphate-buffered saline (PBS) solution. The samples were stored at 4 °C before being stained. Actin filaments were stained with phalloidin at a concentration of 2.5 units/mL dissolved in a 0.1% (v/v) Triton X-100, 1% (w/v) bovine serum albumim (BSA)/PBS solution and left for 1 h in the dark. Then, the glass slides were washed first with a 1% BSA/PBS solution and then with distilled water before being placed on glass supports with 5 μL of a 20 μL/mL 4′,6-diamidino-2-phenylindole (DAPI) solution in Fluoromount (Diagnostic Biosystem) to allow them to dry. Images were acquired with a Nikon Ti2 Eclipse A1 laser confocal microscope and analyzed with a NIS Elements instrument (Nikon).

Visualization of Cell Internalization via Two-Photon-Excited Fluorescence (TPEF). The internalization of unlabeled UCNP-LBMS was also investigated to exclude the influence of surface functionalization on the internalization properties of the NPs. To perform this test, cells were seeded (3×10^5 cells/well in 2 mL) onto quartz slides placed in the wells of a six-well plate. Twenty-four hours after cell seeding, the cell culture medium was replaced with C/S-UCNP-LBMS-60-containing medium at a concentration of 100 μg/mL. Cells were fixed onto the quartz slide following the same procedure described before 1, 4, 24, and 48 h after the administration of NPs.

Before analysis, another quartz slide was placed on top of the one to which cells were affixed. A dual-output rapidly tunable all-fiber optical parametric oscillator (OPO) light source (Picus Duo, Refined Laser Systems) based on a ytterbium-doped fiber oscillator at a repetition rate of 40.5 MHz was employed for imaging. The amplified output pulses from the fiber OPO (tunable from 770 to 980 nm) with a pulse duration of 7 ps were used for excitation. This beam was sent into a home-built vertical microscope to perform imaging via TPEF. The laser was focused via a water-immersion objective with 100× magnification, a 1.25 numerical aperture, and a 0.25 mm working distance (C-Apochromat, Carl Zeiss). The average laser power was kept constant on the sample plane, at 25 mW for all measurements.

The epi-fluorescence photons in the visible range generated by FAD, NAD(P)H, and the nanoparticles were collected in backward scattering by the same objective and isolated from the scattered fundamental excitation laser light using a combination of two short-pass filters at 750 nm (FF01-750/SP-25, Semrock) and 600 nm (FESH0600, Thorlabs). Signals were detected via a photomultiplier tube (R3896, Hamamatsu Photonics).

A raster scan of the sample was realized through a motorized XY translational stage (Standa). Images were acquired using a custom graphical user interface programmed in MATLAB App Designer. For each 80 μm × 80 μm field of view, two consecutive images at 780 nm
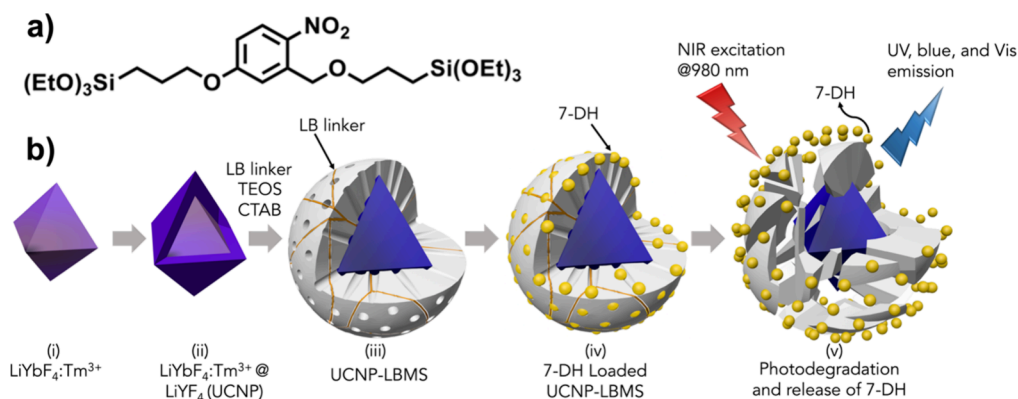
Figure 1. (a) Chemical structure of the LB linker. (b) Schematic illustration of the synthesis of C/S-UCNP-LBMS and subsequent photodegradation and drug release upon NIR irradiation.
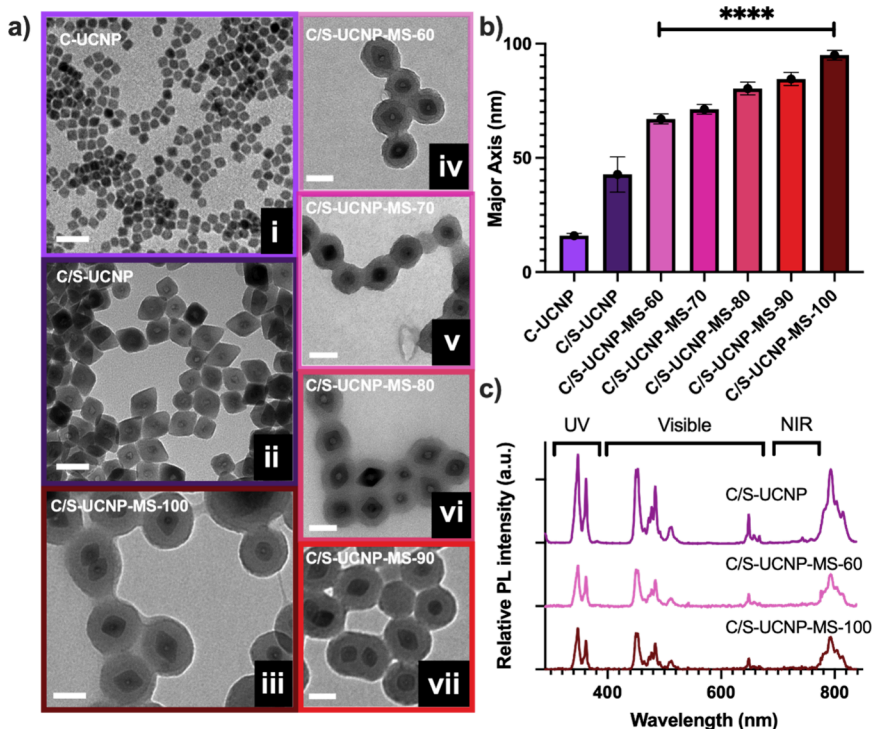

Figure 2. (a) TEM images of (i) C-UCNP, (ii) C/S-UCNP, (iii) C/S-UCNP-MS-100, (iv) C/S-UCNP-MS-60, (v) C/S-UCNP-MS-70, (vi) C/S-UCNP-MS-80, and (vii) C/S-UCNP-MS-90. All scale bars are 50 nm. (b) Average major axis length as calculated from TEM images. Results of one-way ANOVA are shown as ****$p < 0.0001$ ($n = 100$). (c) Upconversion emission spectra (λ_{ex} = 980 nm; 350 W/cm^2) of C/S-UCNP, C/S-UCNP-MS-60, and C/S-UCNP-MS-100. Emission spectra are shown for only the thinnest and thickest shells for the sake of clarity.

and at an excitation wavelength of 980 nm were acquired with 240 pixel × 240 pixel resolution at a pixel dwell time of 1.5 ms.

Statistical Analysis. All data are presented as the mean and standard deviation, and all statistical analysis was performed in GraphPad Prism 8 (GraphPad Software Inc.). For each experiment, the type of statistical test used for the comparison is included in the figure caption. A p value of <0.05 is denoted with one asterisk, and a p value of <0.01 with two asterisks. Breakability tests were fitted with cubic spline curves for ease of visualization. For the drug release experiments, a t test was run on the last time release point to determine the significance. Both the breakability and drug release experiments were performed in triplicate. A two-way analysis of variance (ANOVA) was performed for the in vitro biocompatibility tests to determine significance for different samples across varying concentrations.

RESULTS AND DISCUSSION

Figure 1 illustrates the incorporation of the LB linker (Figure 1a) into the synthesis of C/S-UCNP-LBMS. The synthesis steps are described in detail in Materials and Methods. First, LiYbF$_4$:Tm^{3+} cores (C-UCNP) capped with oleic acid and oleylamine were synthesized using the thermal decomposition method[33] (Figure 1b, i). A Tm doping concentration of 0.5% was chosen to maximize the UV emission as previously demonstrated.[34] To enhance the upconversion emission, the cores were passivated with a LiYF$_4$ shell to obtain LiYbF$_4$:Tm^{3+}@LiYF$_4$ (C/S-UCNP) (Figure 1b, ii). Previous studies[14,35] show that the passive shell acts as a barrier to limit the loss of energy to the surroundings so that most of the excitation energy gathered by the Yb^{3+} ions is channeled to the Tm^{3+} ions. Furthermore, upon passivation of the cores with an
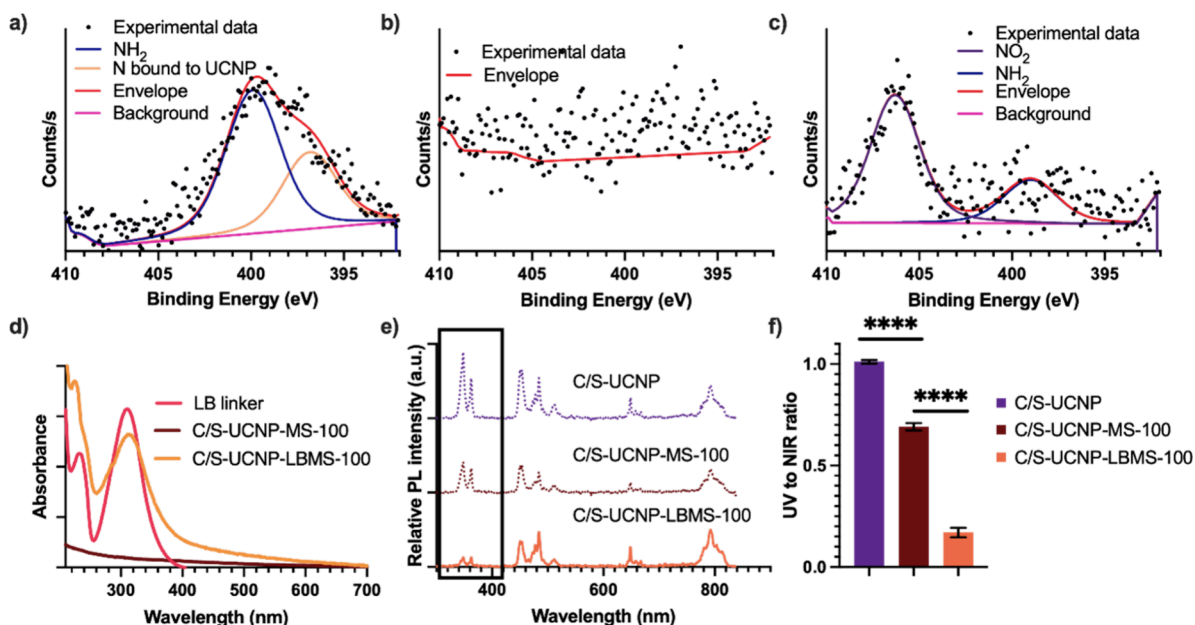
Figure 3. High-resolution XPS N 1s spectra of (a) C/S-UCNP, (b) C/S-UCNP-MS-100, and (c) C/S-UCNP-LBMS-100. (d) UV−vis absorption spectra of the LB linker, C/S-UCNP-MS-100, and C/S-UCNP-LBMS-100 (0.5 mg/mL in EtOH). (e) UC emission spectra (λ_{ex} = 980 nm; 350 W/cm^2) of C/S-UCNP (0.5 mg/mL in hexane), C/S-UCNP-MS-100, and C/S-UCNP-LBMS-100 (1 mg/mL in H$_2$O). Dotted spectra are repeated here from Figure 2c for comparison. (f) Ratio of the integrated UV (335−400 nm) and NIR (730−837 nm) peak areas measured from UC emission spectra shown in panel e (n = 10). Results of an unpaired t test to compare the UV:NIR ratios of C/S-UCNP, C/S-UCNP-MS-100, and C/S-UCNP-LBMS-100 shown as ****$p < 0.0001$.

inert shell, the cation sublattice of the UCNP core can be composed entirely of the sensitizer (Yb^{3+}) ions,[36] thus maximizing excitation light absorption, leading to more emitted UV/NIR radiation than traditional LiYF$_4$:Tm^{3+}, Yb^{3+} UCNPs.[14]

Next, the C/S-UCNPs were rendered hydrophilic and light-breakable by being coated with a LB-integrated mesoporous organosilica-based shell (LBMS), following a reverse microemulsion process previously developed to coat UCNPs with MS[37] (Figure S3). Briefly, CTAB was used as a stabilizing surfactant to transfer the hydrophobic C/S-UCNPs to the aqueous phase as well as the organic template for the formation of the MS shell during the hydrolysis and condensation of TEOS. The LB linker was added during this reaction and co-condensed with the TEOS onto the C/S-UCNP surface to form C/S-UCNP-LBMS (Figure 1b, iii).

Once the system was synthesized and characterized (see the results below), the mesopores were loaded with 7-DH (Figure 1b, iv) and subjected to 980 nm irradiation. Under NIR irradiation, the C/S-UCNP converts the incident NIR light to UV; the LB linker absorbs the UV radiation and is cleaved, resulting in the subsequent breakage of the shell and release of the encapsulated drug (Figure 1b, v).

TEM images of C-UCNP and C/S-UCNP (Figure 2a, i and ii) reveal a uniform size distribution with major axes of 16 ± 1 and 43 ± 8 nm, respectively (Figure 2b). To prepare C/S-UCNP-MS with various silica shell thicknesses, we varied the amount of the TEOS precursor between 60% and 100% of the original volume, which corresponds to a C/S-UCNP:TEOS mass ratio of 1:9 (see Materials and Methods for more details). The shell thickness increased proportionally to the amount of TEOS precursor added, as shown in the TEM images of parts iii−viii of Figure 2a and represented quantitively in Figure 2b.

DLS measurements on C/S-UCNP-MS with various silica shell thicknesses gave a hydrodynamic diameter (D_h) ranging from 220 ± 60 to 330 ± 150 nm and polydispersity indices (PDIs) ranging between 0.33 ± 0.02 and 0.55 ± 0.10 (Figure S4a). We also attempted to use the shell growth time as a measure to control for shell thickness; however, decreasing the growth time from 10 to 5 min did not affect the shell growth but instead resulted in more unstable dispersions as shown by the higher PDI as measured by DLS (Figure S4a,b).

The upconversion emission spectra of C/S-UCNP, C/S-UCNP-MS-60, and C/S-UCNP-MS-100 upon NIR irradiation at 980 nm are shown in Figure 2c. The C/S-UCNP spectra display emission peaks characteristic of Tm^{3+}. The UV emission peaks at 340 and 360 nm correspond to the $^1I_6 \rightarrow$ $^3F_4$ and $^1D_2 \rightarrow {}^3H_6$ transitions, respectively. The three visible peaks at 450, 480, and 660 nm correspond to the $^1D_2 \rightarrow {}^3F_4$, $^1G_4 \rightarrow {}^3H_6$, and $^1G_4 \rightarrow {}^3F_4$ transitions, respectively, and the NIR peak at 790 nm corresponds to the $^1G_4 \rightarrow {}^3H_5$ and $^3H_4 \rightarrow$ $^3H_6$ transitions.[28,34,38] C/S-UCNP-MS-60 and C/S-UCNP-MS-100 show similar peaks, although all peaks were overall less intense than in C/S-UCNP. This decrease in intensity can be mainly attributed to solvent effects as C/S-UCNP-MS were in water while C/S-UCNP were in hexane, and water absorbs more of the incoming 980 nm radiation than do organic solvents.[28,39] The OH groups in water as well as the Si−OH groups in silica also have vibrational modes that can result in an increased level of nonradiative relaxation of the excited states, thus quenching UCNP luminescence.[40] To determine the effect of MS shell thickness on UV emission, we integrated the area under the UV emission peaks normalized against the integrated NIR area and plotted it as a function of increasing silica shell thickness. As shown in Figure S5, the thickness of the silica shell did not significantly affect the UV:NIR ratio.

After we demonstrated the tunability of the silica shell thickness, we covalently embedded the LB linker into the MS shell to form an NIR-responsive system. For the purposes of verifying successful incorporation of the LB linker within the MS shell, all characterization was done on C/S-UCNP-MS-100 and C/S-UCNP-LBMS-100 samples.

X-ray photoelectron spectroscopy (XPS) survey scans were used to detect the change in the elemental surface composition of the UCNPs after the growth of MS and LBMS shells (Figure S6). Yttrium and fluorine present on the C/S-UCNP surface are due to the LiYF$_4$ passive shell, while carbon, nitrogen, and oxygen were attributed to the fatty acid chains from the oleic acid and oleylamine ligands used to stabilize the C/S-UCNP. Upon growth of the MS shell, silicon was detected, and the amount of oxygen significantly increased compared to that in C/S-UCNP due to the Si—O bonds that comprise the MS shell. This increase in oxygen content also resulted in a relative decrease in the level of yttrium and fluorine from the core UCNP. Nitrogen was not detected in C/S-UCNP-MS-100 (Figure 3b) but reappeared in C/S-UCNP-LBMS-100 due to the presence of nitrogen in the LB linker (Figure 3c). The high-resolution N 1s spectrum of C/S-UCNP shows a peak centered around 399.7 eV, which corresponds to the free NH$_2$ groups from the oleylamines, and another peak at 396.6 eV, assigned to the N atom bound to the UCNP surface[41] (Figure 3a). The most intense peak in the C/S-UCNP-LBMS-100 spectra is present at 406.5 eV, confirming the presence of NO$_2$ groups due to the LB linkers within the LBMS shell, while a smaller peak at 399 eV is due to the free NH$_2$ groups from oleylamine (Figure 3c). High-resolution C 1s and O 1s spectra further confirm successful surface modifications (Figure S7). Fourier transform infrared spectroscopy (FTIR) was used as a complementary technique to further confirm the chemical composition of the MS and LBMS shells (Figure S8).

The addition of the organic linker in the LBMS shell was quantified by performing thermogravimetric analysis (TGA) in a N$_2$ atmosphere (Figure S9). The 10% weight loss of C/S-UCNP from 220 to 550 °C can be attributed to the degradation of oleic acid and oleylamine.[42] The additional weight loss observed in C/S-UCNP-MS-100 can be explained by the further condensation of unreacted hydroxyl groups at temperatures of >200 °C within the silica structure,[43,44] while the weight loss difference at 800 °C between C/S-UCNP-MS-100 and C/S-UCNP-LBMS-100 is due to the presence of the organic linker, which is an estimated 4 wt % (Table S1).

UV−vis absorption spectroscopy also confirmed the presence of the LB linker in the C/S-UCNP-LBMS-100 as shown by the characteristic absorption bands at 242 and 320 nm, which are due to the nitrobenzyl group in the linker (Figure 3d).[45] The presence of the LB linker is further shown by the quenching of the UV emission bands (347 and 362 nm) of C/S-UCNP-LBMS-100 (Figure 3e), because the LB linker in the LBMS shell absorbs these bands. The integrated UV:NIR peak ratios are plotted in Figure 3f as a quantitative representation of the quenching of the UV bands compared with the NIR band used as a reference. The overlap between the LB absorbance and the UV emission of C/S-UNCPs, together with the observed quenching of these upconversion lines, suggests that the transfer of energy from C/S-UCNPs to the LB linker can take place to drive photochemistry under NIR excitation.[46−50] As the UV-emitting Tm^{3+} ions are separated by >10 nm from the LB linker molecules within the LBMS shell, this energy transfer is most likely radiative.

To investigate how the incorporation of the LB linker changed the porosity of the MS shell, N$_2$ adsorption−desorption measurements were performed on C/S-UCNP-MS-100 and C/S-UCNP-LBMS-100 samples (Figure S10). Using the Brunauer−Emmett−Teller (BET) method to calculate the specific surface area and the Barrett−Joyner−Halenda (BJH) method for the pore size distribution, we found that C/S-UCNP-LBMS-100 has a larger BET specific surface area (316.5 m^2/g vs 137.6 m^2/g) but a smaller average pore size (4.7 nm vs 17.5 nm) compared to those of C/S-UCNP-MS-100. Results from two trials are reported in Table S2. These findings are in agreement with those of Picchetti et al., who also reported a decrease in the pore diameter (albeit on a smaller scale) upon integration of the LB linker within MS particles,[31,51] and Kruk et al., who showed that the decrease in the pore diameter was more drastic with greater integration of organosilica.[52] The LB linker could be self-polymerizing in the reaction mixture, thus promoting more non-CTAB-templated condensation, which would result in a more disordered pore structure with smaller pores. A disordered pore structure has been shown to increase the estimate of the BET surface area, thus explaining the increase despite the smaller pore size.[53]

Small-angle X-ray scattering (SAXS) analysis was performed to understand the ordering of pores upon incorporation of the LB linker (Figure S11). While the SAXS pattern for C/S-UCNP-MS-100 has a broad peak centered at $q = 1.2$ nm^{-1}, which is indicative of order in the mesoporous phase, no peaks were present in the C/S-UCNP-LBMS-100 SAXS pattern. This trend toward a more disordered mesoporous phase upon integration of an organic linker was also reported by Travaglini et al.,[51] who studied the integration of linkers in MS particles, with a higher content of the organic linker resulting in broader and less intense SAXS peaks. Thus, it appears that the presence of the bulky, hydrophobic, organic LB linker hinders the formation of an ordered mesoporous phase in C/S-UCNP-LBMS-100,[54] confirming our hypothesis presented above.

Once we confirmed the successful integration of the LB linker within the shell, we studied the effect of shell thickness on its degradation by upconverted UV emission. Although shell thickness did not significantly affect UV emission in a C/S-UCNP-MS system, we hypothesized that it may play a role in the ability of the LBMS shell to break in response to upconverted UV light. The thinnest (C/S-UCNP-LBMS-60) and thickest (C/S-UCNP-LBMS-100) shell samples were chosen to compare the shell degradability and drug release.

To ensure the LB linker within the C/S-UCNP-LBMS samples was degrading in response to UV irradiation, we first exposed C/S-UCNP-LBMS-100 [0.5 mg/mL in a 1:1 (v/v) EtOH/H$_2$O mixture] to direct UV irradiation for ≤2 h. The EtOH/H$_2$O solvent mixture was used instead of pure water to rule out the possibility that the observed degradation was related to dissolution of silica in pure water.[55,56] As expected, the absorption band at 320 nm disappeared after irradiation for 15 min, while at the same time, a peak at 352 nm appeared (Figure S12), in agreement with previous studies.[31] This observation can be explained by the light-induced Norrish type II photodegradation of the nitrobenzyl group into the nitrosobenzaldehyde product.[57,58] For these reasons, the peak intensity at 320 nm was chosen to track the photodegradation of the LB linker.

To confirm that NIR light would also induce similar degradation of the particles due to the upconversion from C/S-UCNP, dispersions of C/S-UCNP-LBMS-60 and C/S-UCNP-

LBMS-100 [0.5 mg/mL in 1:1 (v/v) EtOH/H$_2$O mixture] were irradiated with NIR light (λ_{ex} = 980 nm; 1 W/cm^2). Degradation of the LB linker was monitored using UV−vis spectroscopy, while structural degradation of the particles was visualized by using TEM.

UV−vis spectroscopy revealed that upon exposure to NIR irradiation, the spectra of both C/S-UCNP-LBMS-60 and C/S-UCNP-LBMS-100 showed a decrease in the 320 nm peak only in the presence of NIR exposure, indicating the cleavage of the 2-nitrobenzyl group (Figure 4a,b), but did not show the
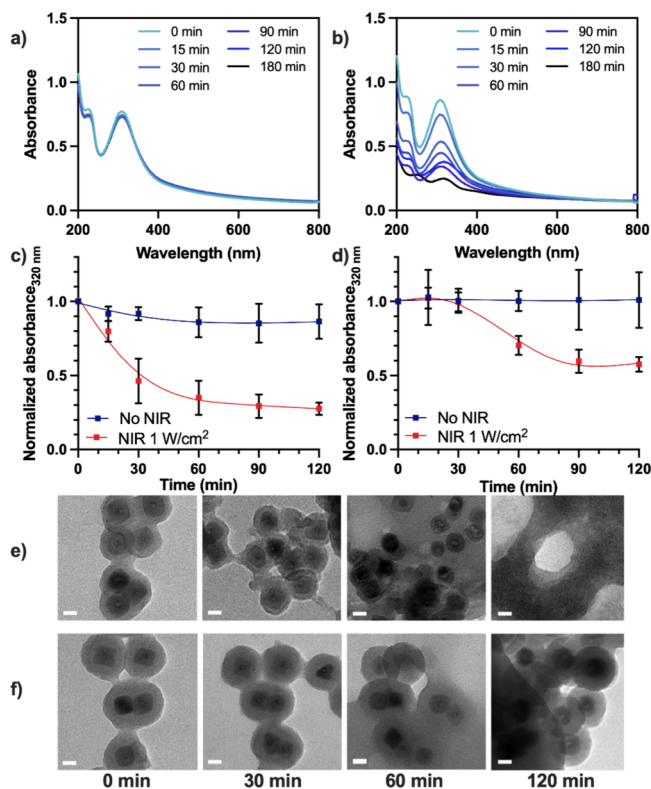
Figure 4. Representative UV−vis absorbance spectra of C/S-UCNP-LBMS-60 (a) without NIR irradiation and (b) with continuous 1 W/cm^2 980 nm NIR irradiation over 3 h. Average absorbance at 320 nm of (c) UCNP-LBMS-60 and (d) UCNP-LBMS-100 [0.5 mg/mL in a 1:1 (v/v) EtOH/H$_2$O mixture] with and without 1 W/cm^2 980 nm irradiation, as measured by UV−vis absorption spectrometry and normalized to the absorbance at time zero. The mean and standard deviation of each time point are recorded (n = 3) and fit to cubic spline curves for ease of visualization. TEM images of (e) C/S-UCNP-LBMS-60 and (f) C/S-UCNP-LBMS-100 taken after 980 nm irradiation for 0, 30, 60, and 120 min of 1 W/cm^2. All scale bars are 50 nm.

appearance of the 352 nm peak as when exposed to UV irradiation. This could be due to the occurrence of side reactions such as the degradation of the nitrosobenzaldehyde photoproduct known to happen in Norrish type II reactions under various conditions.[57,59]

Panels c and d of Figure 4 show a quantitative representation of the absorbance measured at 320 nm with or without exposure to 1 W/cm^2 of 980 nm irradiation of C/S-UCNP-LBMS-60 and C/S-UCNP-LBMS-100. For both particle types, no change in absorbance was observed in the absence of NIR irradiation. Upon NIR irradiation, the absorbance at 320 nm immediately started to decrease for the C/S-UCNP-LBMS-60

sample (Figure 4c), whereas a decrease was observed only after exposure of C/S-UCNP-LBMS-100 for 60 min, indicating slower decay kinetics with a thicker LBMS shell (Figure 4d). The normalized absorbance at 320 nm also reaches a lower value for C/S-UCNP-LBMS-60 after NIR exposure for 120 min as compared to C/S-UCNP-LBMS-100, indicating a higher degree of breakage, which is confirmed by the morphological differences as observed by TEM.

The TEM images taken at each time point show that after irradiation for 60 min, there was significant degradation of the LBMS shell of C/S-UCNP-LBMS-60 (Figure 4e). The LBMS shells were no longer coating the individual particles but had broken down into an amorphous material surrounding multiple UCNPs. After irradiation for 120 min, the silica shell was fully degraded and formed large aggregated masses of particle debris. The reappearance of UCNPs without an LBMS shell confirmed that the aggregates could be attributed to the degraded LBMS shell (Figure S13). The TEM images of C/S-UCNP-LBMS-100 show some degradation with the LBMS shells of individually coated particles merging with one another, as seen at 60 min (Figure 4f). However, at 120 min, many of the LBMS shells were still intact, suggesting that upconverted UV luminescence from NIR irradiation of 1 W/cm^2 over 120 min was not sufficient to fully degrade the shell, as in C/S-UCNP-LBMS-60.

To determine if this difference in shell breakage would affect drug release, we first loaded both C/S-UCNP-LBMS-60 and C/S-UCNP-LBMS-100 with 7-DH and determined the drug loading percent via TGA to be 1.4 and 3.5 wt %, respectively (Table S1). We note that it is very challenging to load hydrophilic mesoporous silica with a hydrophobic drug, hence the low loading capacities. A previous study by Guo et al. has shown that the most effective way to do this is to evaporate the solvent under vacuum to drive the drug into the pores via capillary action,[60] but even with this method, they reported a loading of 9.63% for ZnPc in hollow MS nanoparticles. The even smaller amount found in our work may be explained by the fact that our system lacks the inner cavity of the hollow particles used in the work of Guo et al.

Then, we used a drug release setup as illustrated in Figure 5a (see also NIR- and UV-Triggered Degradation of C/S-UCNP-LBMS) to quantify the amount of 7-DH released into the cyclohexane layer over time with and without NIR irradiation. Changes in the absorbance at λ_{max} = 281 nm (Figure S14) were used to calculate the amount of drug released into the organic layer based on a calibration curve obtained for 7-DH in the same solvent (Figure S15).

Nonspecific release of 7-DH in the absence of NIR irradiation was observed in both C/S-UCNP-LBMS-60 and C/S-UCNP-LBMS-100; this was expected because the mesopores were not capped. A similar level of passive diffusion of 7-DH without light irradiation (∼12 wt %) was also observed in the LBMS particles developed by Picchetti et al.[31] Upon exposure to NIR irradiation, a significant increase in 7-DH release was observed from only C/S-UCNP-LBMS-60 after 3 h (Figure 5b) and not from C/S-UCNP-LBMS-100 (Figure 5c), which we hypothesize is due to the much slower degradation of these particles (Figure 4). While 44 ± 1% of loaded 7-DH was released from C/S-UCNP-LBMS-60 under NIR irradiation, only 13 ± 3% was released from C/S-UCNP-LBMS-100 under the same conditions.

The difference in the amount of drug released from C/S-UCNP-LBMS-60 induced by NIR irradiation at 1 W/cm^2
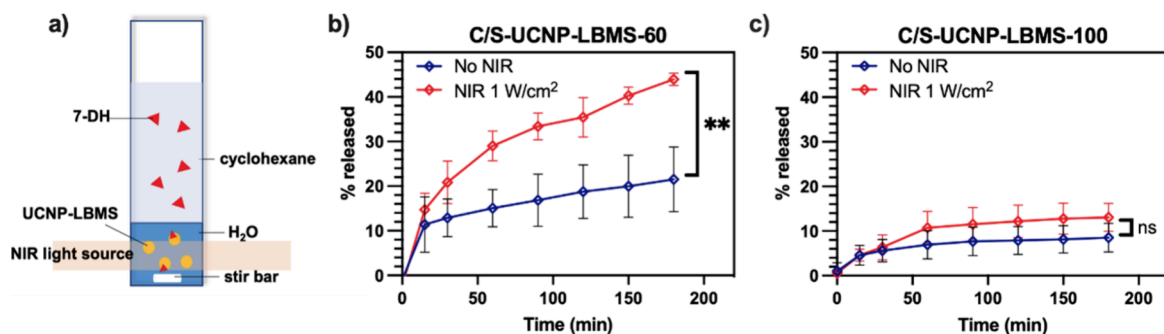
Figure 5. (a) Schematic of the drug release experimental setup. Release of 7-DH from (b) C/S-UCNP-LBMS-60 and (c) C/S-UCNP-LBMS-100 with and without 980 nm NIR irradiation at 1 W/cm². The 7-DH release was monitored using the variation of the absorbance at λ = 281 nm. Results of an unpaired t test at 120 min are shown on the graph as $p > 0.05$ (ns) and $p < 0.01$ (**) (n = 3).
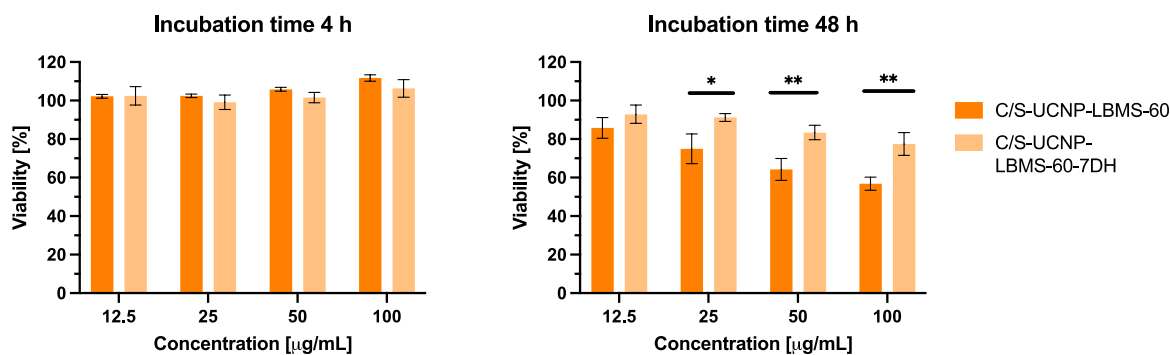
Figure 6. Biocompatibility tests of C/S-UCNP-LBMS-60 and C/S-UCNP-LBMS-60−7DH on HeLa cells with incubation times of 4 and 48 h. Results of two-way ANOVA shown as follows: *$p < 0.05$, **$p < 0.005$, ***$p < 0.001$, and ****$p < 0.0001$ (n = 3).
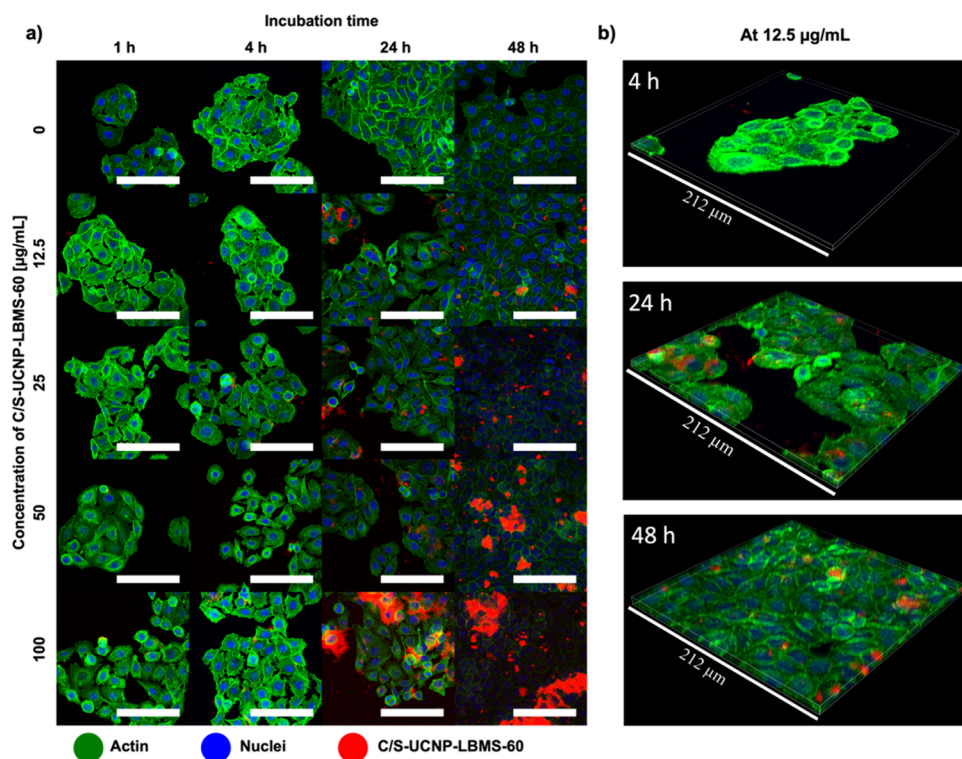
Figure 7. (a) Confocal microscopy visualization of the uptake of C/S-UCNP-LBMS-60 in HeLa cells up to 48 h. Cell nuclei are colored blue, actin filaments in the cytoplasm green, and C/S-UCNP-LBMS-60 red. All scale bars are 100 μm. (b) Three-dimensional reconstruction images of the uptake of C/S-UCNP-LBMS-60 at 12.5 μg/mL from 4 to 48 h.

corresponds to a 2.1-fold increase compared to passive release. In comparison, Picchetti et al. observed a 3-fold increase of 7-DH release compared to passive release when LBMS particles were exposed to direct UV light at 450 W.[31] This comparison

highlights the efficacy of the C/S-UCNP-LBMS-60 system, given that the efficiency of upconversion decreases nonlinearly with higher-order photonic transitions like the NIR-to-UV transition.[61,62]

Next, we chose to further investigate the in vitro biocompatibility and cellular uptake of C/S-UCNP-LBMS-60 to determine its potential for biomedical application. C/S-UCNP-LBMS-60 and C/S-UCNP-LBMS-60 loaded with 7-DH were incubated with HeLa cells at various concentrations (12.5−100 μg/mL) for increasing incubation times (1, 4, 24, and 48 h), and the MTT assay was used to assess biocompatibility (data for incubation times of 1 and 24 h shown in Figure S16). As shown in Figure 6, the HeLa cells are unaffected by the particles upon incubation for 4 h at all NP concentrations. While the incubation time and NP concentration do impact biocompatibility, cell viability did not decrease below 60% even at the highest concentration of 100 μg/mL. The improved biocompatibility upon 7-DH loading could be attributed to the drug's antioxidant activity on cells[63] due to its nonspecific release, as shown in Figure 5.

The cellular uptake of C/S-UCNP-LBMS-60 over time at various NP concentrations is shown in Figure 7a, in which the particles were functionalized with the dye Cy5 for visualization by conventional confocal microscopy. We observed particle internalization starting at 4 h and continuing to increase over 24 and 48 h, similar to the results of previous cellular studies of UCNP uptake.[64] This uptake was visible even at the lowest concentration of 12.5 μg/mL (Figure 7b). At high concentrations (50 and 100 μg/mL), the particles start to form large aggregates that are only partially internalized by the cells; however, there is still a large proportion of particles that have been successfully internalized (Figure S17). The images further suggest that they enter the cell cytoplasm but do not penetrate the membrane of the nucleus. These results were confirmed with TPEF microscopy, where the visible emission from the particles was directly visualized under 980 nm excitation to exclude the effect of Cy5 functionalization on cellular internalization (Figure S18). While the specific setup required for TPEF microscopy limited our ability to observe 7-DH release during 980 nm excitation, especially because 7-DH does not have a fluorescent signal that can be monitored, the in vitro studies presented above provide preliminary data that show that this system may be used for biomedical applications to deliver drugs of interest to target cells.

CONCLUSION

By individually coating UCNPs with a thin LBMS shell, we were able to release a small hydrophobic drug at a low laser power (1 W/cm²) with a 2.1-fold increase in drug release upon NIR irradiation. The one-step functionalization allowed us to synthesize UCNPs with different silica shell thicknesses. We found that a thinner shell increases the rate of NIR-induced LBMS shell degradation and subsequent drug release, leading to short lag times while achieving drug release comparable to that of a UV-activated system. The use of NIR light to trigger drug release, minimal toxicity in HeLa cells, and successful internalization into the cell cytoplasm demonstrate its potential for drug delivery in biological systems.

As opposed to MS coatings that rely on a high power density to activate azobenzene propellers or gatekeeper complexes that merely uncap the mesopores and rely on passive diffusion thereafter, a thin individually coated breakable LBMS coating allows our system to operate at a low power density with greater control over the drug release profile.

As opposed to hydrogel coatings, the choice of an organic silica-based shell structure increases its versatility in the variety of drugs that could be loaded into its pores[60,65,66] and in the possibility of further conjugation with targeting moieties, contrast agents, and performance enhancers via established sol−gel chemistry using alkoxysilanes.[67] In addition, this one-step integration of a light-breakable functionality into a UCNP coating is much simpler than the multistep processes reported in previous systems,[28,68] allowing for greater reproducibility and scalability. All of these are important considerations in the development of future nanoparticles for theranostics.[69] Finally, the ability to tune the efficiency of drug release by tuning the thickness of the photodegradable coating will allow future researchers to design even more efficient photodegradable coatings by ensuring any kind of coating with photobreakable links is within a certain distance of the upconversion core.

This work therefore demonstrates the feasibility of integrating UV-breakable linkers into MS UCNP coatings as a simple and robust way of enabling NIR-triggered drug delivery. By building on simple, reproducible surface functionalization techniques and optimizing the system for operation at laser power densities acceptable for human use,[70] NIR-triggered drug delivery via UCNPs can move closer to becoming a viable option for clinical translation.

AUTHOR INFORMATION

Corresponding Author

Marta Cerruti − *Mining and Materials Engineering, McGill University, Montreal, Quebec H3A 0C5, Canada;* orcid.org/0000-0001-8533-3071; Email: marta.cerruti@mcgill.ca

Authors

Vivienne Tam − *Mining and Materials Engineering, McGill University, Montreal, Quebec H3A 0C5, Canada;* orcid.org/0000-0002-3457-9888

Pierre Picchetti − *Karlsruhe Institute of Technology (KIT), Institute of Nanotechnology (INT), 76344 Eggenstein-Leopoldshafen, Germany;* orcid.org/0000-0002-0689-5998

Yiwei Liu − *Mining and Materials Engineering, McGill University, Montreal, Quebec H3A 0C5, Canada*

Artiom Skripka − *Centre Énergie, Matériaux et Télécommunications, Institut National de la Recherche Scientifique, Université du Québec, Varennes, Québec J3X 1P7, Canada; Nanomaterials for Bioimaging Group, Departamento de Física de Materiales, Facultad de Ciencias, Universidad Autónoma de Madrid, Madrid 28049, Spain; The Molecular Foundry, Lawrence Berkeley National Laboratory, Berkeley, California 94720, United States;* orcid.org/0000-0003-4060-4290

Marco Carofiglio − *Department of Molecular Biochemistry and Pharmacology, Istituto di Ricerche Farmacologiche Mario Negri "IRCCS", 20156 Milan, Italy*

Giulia Tamboia − *Department of Pharmaceutical Sciences, DISFARM, Università degli Studi di Milano, 20133 Milan, Italy; Department of Molecular Biochemistry and Pharmacology, Istituto di Ricerche Farmacologiche Mario Negri "IRCCS", 20156 Milan, Italy; Department of Chemistry, Biology and Biotechnology, University of Perugia, 06123 Perugia, Italy*

Arianna Bresci − *Department of Physics, Politecnico di Milano, 20133 Milan, Italy*

Francesco Manetti − *Department of Physics, Politecnico di Milano, 20133 Milan, Italy*

Giulio Cerullo − *Department of Physics, Politecnico di Milano, 20133 Milan, Italy; CNR-Institute for Photonics and Nanotechnologies (IFN-CNR), 20133 Milan, Italy;* orcid.org/0000-0002-9534-2702

Dario Polli − *Department of Physics, Politecnico di Milano, 20133 Milan, Italy; CNR-Institute for Photonics and Nanotechnologies (IFN-CNR), 20133 Milan, Italy;* orcid.org/0000-0002-6960-5708

Luisa De Cola − *Department of Pharmaceutical Sciences, DISFARM, Università degli Studi di Milano, 20133 Milan, Italy; Department of Molecular Biochemistry and Pharmacology, Istituto di Ricerche Farmacologiche Mario Negri "IRCCS", 20156 Milan, Italy;* orcid.org/0000-0002-2152-6517

Fiorenzo Vetrone − *Centre Énergie, Matériaux et Télécommunications, Institut National de la Recherche Scientifique, Université du Québec, Varennes, Québec J3X 1P7, Canada;* orcid.org/0000-0002-3222-3052

Notes

The authors declare no competing financial interest.

REFERENCES

(1) Tao, Y.; Chan, H. F.; Shi, B.; Li, M.; Leong, K. W. Light: A Magical Tool For Controlled Drug Delivery. *Adv. Funct. Mater.* **2020**, *30*, 2005029.

(2) Barhoumi, A.; Liu, Q.; Kohane, D. S. Ultraviolet Light-Mediated Drug Delivery: Principles, Applications, And Challenges. *J. Controlled Release* **2015**, *219*, 31−42.

(3) Chen, G.; Qiu, H.; Prasad, P. N.; Chen, X. Upconversion Nanoparticles: Design, Nanochemistry, And Applications In Theranostics. *Chem. Rev.* **2014**, *114*, 5161−5214.

(4) Frangioni, J. V. In Vivo Near-Infrared Fluorescence Imaging. *Curr. Opin. Chem. Biol.* **2003**, *7*, 626−634.

(5) Meinhardt, M.; Krebs, R.; Anders, A.; Heinrich, U.; Tronnier, H. Wavelength-Dependent Penetration Depths Of Ultraviolet Radiation In Human Skin. *J. Biomed. Opt.* **2008**, *13*, 044030.

(6) Chen, G.; et al. (A-Naybf 4:Tm 3+)/Caf 2 Core/Shell Nanoparticles With Efficient Near-Infrared To Near-Infrared Upconversion For High-Contrast Deep Tissue Bioimaging. *ACS Nano* **2012**, *6*, 8280−8287.

(7) Zhu, X.; Su, Q.; Feng, W.; Li, F. Anti-Stokes Shift Luminescent Materials For Bio-Applications. *Chem. Soc. Rev.* **2017**, *46*, 1025−1039.

(8) Werts, M. H. V. Making Sense Of Lanthanide Luminescence. *Sci. Prog.* **2005**, *88*, 101−131.

(9) Bixler, J. N.; et al. Assessment Of Tissue Heating Under Tunable Near-Infrared Radiation. *J. Biomed. Opt.* **2014**, *19*, 070501.

(10) Li, Y.; et al. A Versatile Imaging And Therapeutic Platform Based On Dual-Band Luminescent Lanthanide Nanoparticles Toward Tumor Metastasis Inhibition. *ACS Nano* **2016**, *10*, 2766−2773.

(11) Zhan, Q.; et al. Using 915 Nm Laser Excited Tm3+/Er3+/Ho 3+-Doped Naybf4 Upconversion Nanoparticles For In Vitro And Deeper In Vivo Bioimaging Without Overheating Irradiation. *ACS Nano* **2011**, *5*, 3744−3757.

(12) Xie, X.; et al. Mechanistic Investigation Of Photon Upconversion In Nd3+- Sensitized Core-Shell Nanoparticles. *J. Am. Chem. Soc.* **2013**, *135*, 12608−12611.

(13) Johnson, N. J. J.; et al. Direct Evidence For Coupled Surface And Concentration Quenching Dynamics In Lanthanide-Doped Nanocrystals. *J. Am. Chem. Soc.* **2017**, *139*, 3275−3282.

(14) Cheng, T.; Marin, R.; Skripka, A.; Vetrone, F. Small And Bright Lithium-Based Upconverting Nanoparticles. *J. Am. Chem. Soc.* **2018**, *140*, 12890−12899.

(15) Jalani, G.; Tam, V.; Vetrone, F.; Cerruti, M. Seeing, Targeting And Delivering With Upconverting Nanoparticles. *J. Am. Chem. Soc.* **2018**, *140*, 10923−10931.

(16) Xiang, J.; et al. Nanocomplexes Of Photolabile Polyelectrolyte And Upconversion Nanoparticles For Near-Infrared Light-Triggered Payload Release. *ACS Appl. Mater. Interfaces* **2018**, *10*, 20790−20800.

(17) Luo, Y. H.; et al. Bidirectional Photoswitching Via Alternating NIR And UV Irradiation On A Core-Shell UCNP-SCO Nanosphere. *ACS Appl. Mater. Interfaces* **2018**, *10*, 16666−16673.

(18) Shao, Y.; et al. Engineering Of Upconverted Metal-Organic Frameworks For Near-Infrared Light-Triggered Combinational Photodynamic/Chemo-/Immunotherapy Against Hypoxic Tumors. *J. Am. Chem. Soc.* **2020**, *142*, 3939−3946.

(19) Kamaly, N.; Xiao, Z.; Valencia, P. M.; Radovic-Moreno, A. F.; Farokhzad, O. C. Targeted Polymeric Therapeutic Nanoparticles: Design, Development And Clinical Translation. *Chem. Soc. Rev.* **2012**, *41*, 2971−3010.

(20) Fomina, N.; Mcfearin, C.; Sermsakdi, M.; Edigin, O.; Almutairi, A. UV And Near-IR Triggered Release From Polymeric Nanoparticles. *J. Am. Chem. Soc.* **2010**, *132*, 9540−9542.

(21) Son, S.; Shin, E.; Kim, B. S. Light-Responsive Micelles Of Spiropyran Initiated Hyperbranched Polyglycerol For Smart Drug Delivery. *Biomacromolecules* **2014**, *15*, 628−634.

(22) Croissant, J. G.; Fatieiev, Y.; Khashab, N. M. Degradability And Clearance Of Silicon, Organosilica, Silsesquioxane, Silica Mixed Oxide, And Mesoporous Silica Nanoparticles. *Adv. Mater.* **2017**, *29*, n/a.

(23) Vallet-Regí, M.; Balas, F.; Arcos, D. Mesoporous Materials For Drug Delivery. *Angew. Chemie - Int. Ed.* **2007**, *46*, 7548−7558.

(24) Liu, J.; Bu, W.; Pan, L.; Shi, J. NIR-Triggered Anticancer Drug Delivery By Upconverting Nanoparticles With Integrated Azobenzene-Modified Mesoporous Silica. *Angew. Chem., Int. Ed.* **2013**, *52*, 4375.

(25) Yang, Y.; Velmurugan, B.; Liu, X.; Xing, B. NIR Photoresponsive Crosslinked Upconverting Nanocarriers Toward Selective Intracellular Drug Release. *Small* **2013**, *9*, 2937−2944.

(26) Zhao, L.; et al. Near-Infrared Photoregulated Drug Release In Living Tumor Tissue Via Yolk-Shell Upconversion Nanocages. *Adv. Funct. Mater.* **2014**, *24*, 363−371.

(27) Kumar, B.; Murali, A.; Mattan, I.; Giri, S. Near-Infrared-Triggered Photodynamic, Photothermal, And On Demand Chemotherapy By Multifunctional Upconversion Nanocomposite. *J. Phys. Chem. B* **2019**, *123*, 3738−3755.

(28) Jalani, G.; et al. Photocleavable Hydrogel-Coated Upconverting Nanoparticles: A Multifunctional Theranostic Platform For NIR Imaging And On-Demand Macromolecular Delivery. *J. Am. Chem. Soc.* **2016**, *138*, 1078−1083.

(29) Li, J.; Mooney, D. J. Designing Hydrogels For Controlled Drug Delivery. *Nat. Rev. Mater.* **2018**, *1*, 16071.

(30) Gu, D.; et al. Expert Opinion On Drug Delivery Hydrogels With Smart Systems For Delivery Of Hydrophobic Drugs Hydrogels With Smart Systems For Delivery Of Hydrophobic Drugs. *Expert Opin. Drug Delivery* **2017**, *14*, 879−895.

(31) Picchetti, P.; et al. Breaking With Light: Stimuli-Responsive Mesoporous Organosilica Particles. *Chem. Mater.* **2020**, *32*, 392−399.

(32) Li, C.; et al. A Facile Fabrication Of Upconversion Luminescent And Mesoporous Core-Shell Structured B-Nayf4:Yb3+, Er3+@Msio 2 Nanocomposite Spheres For Anti-Cancer Drug Delivery And Cell Imaging. *Biomater. Sci.* **2013**, *1*, 213−223.

(33) Boyer, J.-C.; Vetrone, F.; Cuccia, L. A.; Capobianco, J. A. Synthesis Of Colloidal Upconverting Nayf 4 Nanocrystals Doped With Er 3 + , Yb 3 + And Tm 3 + , Yb 3 + Via Thermal Decomposition Of Lanthanide Trifluoroacetate Precursors. *J. Am. Chem. Soc.* **2006**, *128*, 7444−7445.

(34) Mahalingam, V.; Vetrone, F.; Naccache, R.; Speghini, A.; Capobianco, J. A. Colloidal Tm3+/Yb3+-Doped Liyf4 Nanocrystals: Multiple Luminescence Spanning The UV To NIR Regions Via Low-Energy Excitation. *Adv. Mater.* **2009**, *21*, 4025−4028.

(35) Würth, C.; Fischer, S.; Grauel, B.; Alivisatos, A. P.; Resch-Genger, U. Quantum Yields, Surface Quenching, And Passivation Efficiency For Ultrasmall Core/Shell Upconverting Nanoparticles. *J. Am. Chem. Soc.* **2018**, *140*, 4922−4928.

(36) Zou, Q.; et al. Cooperative And Non-Cooperative Sensitization Upconversion In Lanthanide-Doped Liybf4 Nanoparticles. *Nanoscale* **2017**, *9*, 6521−6528.

(37) Liu, J.; et al. Controlled Synthesis Of Uniform And Monodisperse Upconversion Core/Mesoporous Silica Shell Nano-composites For Bimodal Imaging. *Chem. - A Eur. J.* **2012**, *18*, 2335−2341.

(38) Quintanilla, M.; Cantarelli, I. X.; Pedroni, M.; Speghini, A.; Vetrone, F. Intense Ultraviolet Upconversion In Water Dispersible Srf2:Tm3+,Yb3+ Nanoparticles: The Effect Of The Environment On Light Emissions. *J. Mater. Chem. C* **2015**, *3*, 3108−3113.

(39) Wiesholler, L. M.; et al. Yb,Nd,Er-Doped Upconversion Nanoparticles: 980 Nm: Versus 808 Nm Excitation. *Nanoscale* **2019**, *11*, 13440−13449.

(40) Arppe, R.; et al. Quenching Of The Upconversion Luminescence Of Nayf4:Yb3+,Er3+ And Nayf4:Yb3+,Tm3+ Nano-phosphors By Water: The Role Of The Sensitizer Yb3+ In Non-Radiative Relaxation. *Nanoscale* **2015**, *7*, 11746−11757.

(41) Shi, Y.; et al. Oleylamine-Functionalized Palladium Nano-particles With Enhanced Electrocatalytic Activity For The Oxygen Reduction Reaction. *J. Power Sources* **2014**, *246*, 356−360.

(42) Zhang, T.; Ge, J.; Hu, Y.; Yin, Y. A General Approach For Transferring Hydrophobic Nanocrystals Into Water. *Nano Lett.* **2007**, *7*, 3203−3207.

(43) Kunc, F.; et al. Quantification Of Surface Functional Groups On Silica Nanoparticles: Comparison Of Thermogravimetric Analysis And Quantitative NMR. *Analyst* **2019**, *144*, 5589−5599.

(44) Marszewski, M.; et al. Effect Of Surface Hydroxyl Groups On Heat Capacity Of Mesoporous Silica. *Appl. Phys. Lett.* **2018**, *112*, 2019031.

(45) Zhao, H.; Sterner, E. S.; Coughlin, E. B.; Theato, P. O-Nitrobenzyl Alcohol Derivatives: Opportunities In Polymer And Materials Science. *Macromolecules* **2012**, *45*, 1723−1736.

(46) Skripka, A.; et al. Decoupling Theranostics With Rare Earth Doped Nanoparticles. *Adv. Funct. Mater.* **2019**, *29*, 1807105.

(47) Dawson, P.; Romanowski, M. Excitation Modulation Of Upconversion Nanoparticles For Switch-Like Control Of Ultraviolet Luminescence. *J. Am. Chem. Soc.* **2018**, *140*, 5714−5718.

(48) Zuo, J.; et al. Near Infrared Light Sensitive Ultraviolet-Blue Nanophotoswitch For Imaging-Guided 'Off-On' Therapy. *ACS Nano* **2018**, *12*, 3217−3225.

(49) Sanders, S. N.; et al. Triplet Fusion Upconversion Nano-capsules For Volumetric 3D Printing. *Nature* **2022**, *604*, 474−478.

(50) Chen, S.; et al. Near-Infrared Deep Brain Stimulation Via Upconversion Nanoparticle − Mediated Optogenetics. *Science* **2018**, *359*, 679−684.

(51) Travaglini, L.; Picchetti, P.; Totovao, R.; Prasetyanto, E. A.; De Cola, L. Highly Degradable Imine-Doped Mesoporous Silica Particles. *Mater. Chem. Front.* **2019**, *3*, 111−119.

(52) Kruk, M.; Asefa, T.; Jaroniec, M.; Ozin, G. A. Metamorphosis Of Ordered Mesopores To Micropores: Periodic Silica With Unprecedented Loading Of Pendant Reactive Organic Groups Transforms To Periodic Microporous Silica With Tailorable Pore Size. *J. Am. Chem. Soc.* **2002**, *124*, 6383−6392.

(53) Zou, J.; et al. A Preliminary Study On Assessing The Brunauer-Emmett-Teller Analysis For Disordered Carbonaceous Materials. *Microporous Mesoporous Mater.* **2021**, *327*, 111411.

(54) Kondrashova, N.; Saenko, E.; Lebedeva, I.; Valtsifer, V.; Strelnikov, V. Effect Of Organic-Silane Additives On Textural-Structural Properties Of Mesoporous Silicate Materials. *Microporous Mesoporous Mater.* **2012**, *153*, 275−281.

(55) Möller, K.; Bein, T. Degradable Drug Carriers: Vanishing Mesoporous Silica Nanoparticles. *Chem. Mater.* **2019**, *31*, 4364−4378.

(56) Pham, A. L.-T.; Sedlak, D. L.; Doyle, F. M. Dissolution Of Mesoporous Silica Supports In Aqueous Solutions: Implications For Mesoporous Silica-Based Water Treatment Processes. *Appl. Catal., B* **2012**, *126*, 258−264.

(57) Romano, A.; Roppolo, I.; Rossegger, E.; Schlögl, S.; Sangermano, M. Recent Trends In Applying Ortho-Nitrobenzyl Esters For The Design Of Photo-Responsive Polymer Networks. *Materials* **2020**, *13*, 2777.

(58) Klán, P.; et al. Photoremovable Protecting Groups In Chemistry And Biology: Reaction Mechanisms And Efficacy. *Chem. Rev.* **2013**, *113*, 119−191.

(59) Abou Nakad, E.; Bolze, F.; Specht, A. O-Nitrobenzyl Photoremovable Groups With Fluorescence Uncaging Reporting Properties. *Org. Biomol. Chem.* **2018**, *16*, 6115−6122.

(60) Guo, L.; et al. A Comprehensive Study Of Drug Loading In Hollow Mesoporous Silica Nanoparticles: Impacting Factors And Loading Efficiency. *Nanomaterials* **2021**, *11*, 1293.

(61) Arppe, R.; et al. Quenching Of The Upconversion Luminescence Of Nayf4:Yb3+,Er3+ And Nayf4:Yb3+,Tm3+ Nano-phosphors By Water: The Role Of The Sensitizer Yb3+ In Non-Radiative Relaxation. *Nanoscale* **2015**, *7*, 11746−11757.

(62) Liu, G. Advances In The Theoretical Understanding Of Photon Upconversion In Rare-Earth Activated Nanophosphors. *Chem. Soc. Rev.* **2015**, *44*, 1635−1652.

(63) Delahunty, I.; et al. 7-Dehydrocholesterol Encapsulated Polymeric Nanoparticles As A Radiation-Responsive Sensitizer For Enhancing Radiation Therapy. *Small* **2022**, *18*, e2200710.

(64) Voronovic, E.; et al. Uptake Of Upconverting Nanoparticles By Breast Cancer Cells: Surface Coating Versus The Protein Corona. *ACS Appl. Mater. Interfaces* **2021**, *13*, 39076−39087.

(65) Tang, F.; Li, L.; Chen, D. Mesoporous Silica Nanoparticles: Synthesis, Biocompatibility And Drug Delivery. *Adv. Mater.* **2012**, *24*, 1504−1534.

(66) Mamaeva, V.; Sahlgren, C.; Lindén, M. Mesoporous Silica Nanoparticles In Medicine-Recent Advances. *Adv. Drug Delivery Rev.* **2013**, *65*, 689−702.

(67) Liberman, A.; Mendez, N.; Trogler, W. C.; Kummel, A. C. Synthesis And Surface Functionalization Of Silica Nanoparticles For Nanomedicine. *Surf. Sci. Rep.* **2014**, *69*, 132−158.

(68) Liu, J.; Bu, W.; Pan, L.; Shi, J. NIR-Triggered Anticancer Drug Delivery By Upconverting Nanoparticles With Integrated Azoben-zene-Modified Mesoporous Silica **. *Angew. Chem., Int. Ed. Engl.* **2013**, *52*, 4375−4379.

(69) Wu, F.; et al. Molecular Engineering Of Surface Functional Groups Enabling Clinical Translation Of Nanoparticle-Drug Conjugates. *Chem. Mater.* **2022**, *34*, 5344−5355.

(70) Fedele, D.; Fusi, F. Thermal Effects of NIR Laser Radiation In Biological Tissue: A Brief Survey. *Energy Health* **2010**, *06*, 10−15.